First-principles characterization of a heteroceramic interface: ZrO2(001) deposited on an alpha-Al2O3(1(1)over-bar02) substrate

Christensen, Asbjørn; Carter, Emily A.

Published in:
Physical Review B (Condensed Matter and Materials Physics)

Link to article, DOI:
10.1103/PhysRevB.62.16968

Publication date:
2000

Document Version
Publisher's PDF, also known as Version of record

Citation (APA):
Christensen, A., & Carter, E. A. (2000). First-principles characterization of a heteroceramic interface: ZrO2(001) deposited on an alpha-Al2O3(1(1)over-bar02) substrate. Physical Review B (Condensed Matter and Materials Physics), 62(24), 16968-16983. DOI: 10.1103/PhysRevB.62.16968

PHYSICAL REVIEW B VOLUME 62, NUMBER 24 15 DECEMBER 2000-II

First-principles characterization of a heteroceramic interface: $ZrO_2(001)$ deposited on an α-$Al_2O_3(1\bar{1}02)$ substrate

A. Christensen*

Department of Chemistry and Biochemistry, Box 951569, University of California, Los Angeles, California 90095-1569
and Center for Atomic-scale Materials Physics (CAMP), Department of Physics, Technical University of Denmark, Bygning 307,
DK-2800 Lyngby, Denmark

Emily A. Carter†

Department of Chemistry and Biochemistry, Box 951569, University of California, Los Angeles, California 90095-1569

(Received 27 December 1999)

We have studied an alumina/zirconia interface using the all-electron projector augmented wave formalism within density functional theory. We present the electronic, structural, and energetic properties of the $ZrO_2(001)/\alpha$-$Al_2O_3(1\bar{1}02)$ interface as well as of the free α-$Al_2O_3(1\bar{1}02)$ and $ZrO_2(001)$ surfaces. We find that the generalized gradient correction significantly lowers the oxide surface energies, compared to values obtained by the local density approximation. The monoclinic-tetragonal transition in $ZrO_2(001)$ thin films is discussed as well as strain effects involved in the interface formation. The stoichiometric alumina/zirconia interface is found to be weakly bonded, regardless of the film thickness, and the $ZrO_2(001)/\alpha$-$Al_2O_3(1\bar{1}02)$ interface has a rather epitaxial character, due to a low lattice mismatch of $\sim 4\%$. The impact of such weak interactions on ceramic coating stability is discussed.

I. INTRODUCTION

Characterization of the properties of crystalline interfaces between metals and ceramics, as well as heterogeneous interfaces between two ceramics, is of both fundamental interest—little is understood about the atomic level interactions at such interfaces[1]—and practical interest—these are the interfaces present in so-called thermal barrier coatings (TBC's). These coatings are used to protect gas turbine engine components found in both aircraft and stationary power plants. The protective coatings allow fuel combustion to be carried out at the highest possible operating temperature (maximizing fuel efficiency).[2] Current TBC's fail after a sequence of heating and cooling cycles.[3]

Zirconia-based materials are often chosen for TBC's, due to their high melting temperature, low thermal conductivity, similar coefficient of thermal expansion to that of the Ni superalloy used to construct the engine parts, and excellent corrosion and thermal shock resistance.[4,5] The main drawback of pure zirconia is the tetragonal-monoclinic phase transformation induced by thermal cycling. This transition is accompanied by a volume expansion[6,7] of $\sim 4\%$, which generates cracks and eventually de-adhesion of the TBC. The tetragonal-monoclinic transition is suppressed by adding cubic oxides in small amounts ($\sim 8.5\%$) to zirconia.[8,9] Still, TBC's are prone to thermal cycling fatigue, due to unequal thermal expansion of the metal and the TBC, which causes the TBC to spall as a result of thermally induced stresses.[3] Another contributing mechanism to the spallation is oxidation of the TBC/metal interface. The spallation problem is often reduced by placing a bond coat in between the TBC and the metal, but under real life operating conditions, the bond coat is oxidized.[10,11] Therefore, a lot of effort[2,3] has been put into refining and optimizing TBC/bond coat/metal structures to meet engineering requirements. The search for design principles has hitherto been rather phenomenological; this is a consequence of the structural and chemical complexity of the TBC/bond coat/metal structures, together with the lack of nondestructive experimental probes for *in situ* atomic scale characterization of buried interfaces, let alone oxide surfaces.

Atomistic modeling offers microscopic insight into otherwise inaccessible aspects of complex interface structures. Our group currently has a concerted effort to characterize, within ideal model interfaces, the interactions between different materials where they meet. In this paper, we focus on the ZrO_2/α-Al_2O_3 interface, which is relevant at the TBC/bond coat interface, when the Ni-Al-Cr-Y bond coat is oxidized. Also, this interface determines mechanical and thermal properties of technologically important ZrO_2/Al_2O_3 composites. α-alumina is thought to form at the TBC/bond coat junction, but other forms of Al_2O_3 may form (like γ-Al_2O_3). However, since α-Al_2O_3 is the most stable phase and other Al_2O_3 phases have a more complex, mostly ill-characterized bulk structure, we restrict ourselves to study α-Al_2O_3 only.

We have also examined the Al_2O_3/Ni interaction,[12] where we learn that Al_2O_3 may be responsible for the spallation that occurs. We have also studied the ZrO_2/Ni(111) interface[13] to understand on an atomistic level why the bond coat is necessary at all between the TBC and a Ni-rich superalloy. We also previously studied the bulk and surface phases of all ZrO_2 phases.[14] Here, we concluded that the t-$ZrO_2(111)$ and the m-$ZrO_2(\bar{1}11)$ surfaces are most stable. This had implications for the tetragonal-monoclinic transition in ZrO_2 nanoparticles. Recently Stapper and co-workers[15] modeled defects in bulk yttria-stabilized ZrO_2 (YSZ) using the local-density approximation (LDA) in an

0163-1829/2000/62(24)/16968(16)/$15.00

96-atom unit cell and obtained insight into localized electronic states in the material.

Many experiments of ZrO_2 and YSZ film growth on an α-Al_2O_3 substrate have been reported. This epitaxial system is also used as a substrate for ceramic high-T_c superconductors, where the zirconia film acts as a chemical buffer layer.[16–18] On the α-$Al_2O_3(1\bar{1}02)$ substrate, m-$ZrO_2(001)$[16,19] and YSZ(001)[16,19,17] have been observed to grow. However, at high oxygen pressure[16] or substrate temperatures[17] beyond 950 °C, YSZ(111)/α-$Al_2O_3(1\bar{1}02)$ growth was detected. On the α-$Al_2O_3(11\bar{2}0)$ and α-$Al_2O_3(0001)$ substrates, YSZ(001) growth was observed.[18,20] For fast deposition rates, Moulzolf *et al.*[21] observed m-$ZrO_2(001)/\alpha$-$Al_2O_3(10\bar{1}2)$ growth. However, for slow deposition rates, they observed c-$ZrO_2(001)/\alpha$-$Al_2O_3(10\bar{1}2)$ growth for up to 400 Å ZrO_2 films (*vide infra*). Scanlan *et al.*[22] studied growth of dense ZrO_2/Al_2O_3 nanolaminate structures. The Al_2O_3 layers were amorphous, whereas the ZrO_2 layers were polycrystalline. For thick ZrO_2 films, polycrystalline m-$ZrO_2(\bar{1}11)$ growth was observed. However, for thin ZrO_2 films, polycrystalline t-$ZrO_2(111)$ growth took place. Although the Al_2O_3 confines the ZrO_2 such that the tetragonal-monoclinic transformation is suppressed, it remains to be shown that the confined t-ZrO_2 layers are stable upon thermal cycling.

This paper is organized as follows: In Sec. II, we discuss the calculational details of our paper. In Sec. III, we discuss the structure and electronic properties of the bulk phases α-Al_2O_3 and ZrO_2. Then, in Sec. IV B, we present results for the clean oxide surfaces and then for the alumina/zirconia interface, which is the main concern of this paper. In Sec. V, we relate our calculated results to experiments, and finally in Sec. VI, we draw conclusions from our paper.

II. COMPUTATIONAL ASPECTS

In this paper, we study the ZrO_2/α-Al_2O_3 interface using the all-electron projector augmented wave (PAW) method, which was proposed by Blöchl[23] for solving the Kohn-Sham equations within density-functional theory[24] (DFT). The PAW formalism has the numerical advantages of pseudopotential techniques while retaining the physics of all-electron methods. This relatively new technique has proven very accurate in comparison with other *ab initio* methods[23,25,26] within the DFT framework.

A. Electronic structure

The key element in the PAW formalism is the set of projection operators that establish the transformation between the physical all-electron wave-function Hilbert space and the pseudowave-function Hilbert space, where electronic states are represented conveniently in a plane-wave basis. The PAW projection operators used in this paper were generated as described by Blöchl.[23] For Al, one projector is used for each of the *s*, *p*, and *d* channels, with pseudowave form parameters (see Blöchl[23] for details) $r_k = 1.8\ a_0$ and $\lambda = 6$. For O, one projector is used for each of the *s* and *p* channels, with $r_k = 1.0\ a_0$ and $\lambda = 6$. For Zr, one projector for each of the *s* and *p* channels and two projectors for the *d* channels are used, all with $r_k = 2.0\ a_0$ and $\lambda = 6$. All atomic pseudopartial waves for the PAW-projector construction are generated at the atomic eigenvalue for the corresponding angular momentum channel. The auxiliary pseudowave for the Zr *d* channel is placed at the atomic vacuum level. No Zr semicore states are treated as valence in our calculation. A very accurate description of the energetics in a pure Zr metal crystal requires inclusion of the $(4s,4p)$ core states, which are rather extended and overlap slightly with $(4s,4p)$ core states at neighboring Zr ions. However, in ZrO_2, Zr atoms only have O ions as nearest neighbors and consequently the $Zr(4s,4p)$ states can only hybridize with O states. In ZrO_2, all O resonances are well separated in energy from the $Zr(4s,4p)$ resonances[27] and therefore the O-$Zr(4s,4p)$ hybridization is weak. Thus we expect the frozen-core approximation, which underlies the PAW implementation used in the present paper, to be accurate for ZrO_2, even if the $Zr(4s,4p)$ states are treated as core states. We will deal with this in more detail elsewhere.[13]

All calculations we present in this paper, including atomic reference data for the PAW setup, were performed within a generalized gradient approximation (GGA) for exchange and correlation. More precisely, the nonspin polarized local density approximation (LDA) functional, as parametrized by Perdew and Zunger,[28] is used in conjunction with gradient corrections for exchange, as proposed by Becke,[29] and gradient corrections for correlation, as proposed by Perdew.[30] For our slab calculations (surfaces and interfaces), we use a $2\times2\times1$ grid for sampling the Brillouin-zone integrals, corresponding to a reciprocal space sampling density of ~ 0.6 Å^{-1}. For bulk α-Al_2O_3 and c-ZrO_2 reference and test calculations, we use the same *k*-point sampling density, corresponding to a $2\times2\times2$ grid. This k-point sampling density is the standard choice for insulating systems as Al_2O_3, ZrO_2, and the surfaces and interfaces of these ceramics. Separated surface calculations (to determine interface cohesion) are performed in the same unit cells as the interface calculations to enhance error cancellation for the residual *k*-point sampling error. All slab and bulk calculations we present in this paper are performed spin restricted, which is exact for simple oxides like Al_2O_3 and ZrO_2, since the electrons in these systems are spin-paired completely.

The kinetic-energy cutoff for the plane-wave basis is chosen to be 30 Ry (408 eV), corresponding to a convergence of absolute total energies to within 0.2 eV/atom (but where energy differences are essentially converged). The pseudodensity is represented on a grid corresponding to twice the kinetic-energy cutoff of the electronic wave functions. In all our calculations, six empty bands are included, to improve the convergence rate of the eigenstates in the band-gap region.

To interpret the electronic spectra, the atom-projected density-of-states (DOS) is generated by projecting the Kohn-Sham wave functions onto spherical harmonics inside spheres centered on ions. These spheres have the same radii for each species in all our calculations: r(Zr) = 1.60 Å, r(Al) = 1.30 Å, and $r(\mathrm{O}) = 0.81$ Å. This corresponds to weakly overlapping (but not space-filling) spheres for both oxides. These radii correspond to the covalent radius multiplied by a factor of 1.1053, which is the ratio between the radii of space filling to touching spheres in an fcc crystal;

this is a standardized choice in the PAW code. For charge distribution analysis, ionic charges are calculated by integration inside spheres of the atom-projected DOS. This approach for projecting/partitioning collective quantities as charge and energy in a solid is not absolute and only differences are indicative for changes in the local chemistry. For visual convenience, a Gaussian broadening of $\Delta E = 0.5$ eV is performed for all DOS spectra displayed in this paper.

B. Ionic and electronic relaxation

1. Structural quenching

Ions are relaxed to the equilibrium configuration in the slab unit cells using 2nd order damped molecular dynamics in the Car-Parrinello (CP) framework,[31] i.e., ionic and electronic degrees of freedom are relaxed simultaneously using a fictitious Lagrangian (with a viscosity term added to the equation of motion for quenching). The friction term is adaptive, i.e., the viscosity coefficient is decreased as the ground state is approached, so that the system does not get stuck close to the minimum; variable friction also ensures that the entire frequency spectrum is being damped efficiently. The Car-Parrinello equations of motion are integrated by the Verlet algorithm[32] with a time step of 7 a.u. = 0.17 fs. The quench time for our slab systems is in the range 0.1–1.2 ps, including the initial descent of the electronic wave functions to the Born-Oppenheimer surface. Ions are relaxed to a precision of 10 meV per unit cell.

Apart from periodic boundary conditions on the unit cell, no symmetry or constraints are imposed on the electronic density and ionic motion. The unit cells (lattice constants and cell angles) for interface structures considered are not relaxed, but fixed to the values derived from the fully relaxed bulk unit cell of our substrate α-Al_2O_3, described in Sec. III. Including relaxation of slab unit cells parallel to the surface/interface is undesirable when the structures are intended to represent bulk terminations. Further, unit-cell relaxation based on the quantum-mechanical stress theorem[33] is associated with calculational problems, like artificial Pulay stresses.[34] (For our bulk calculations, we circumvent these problems by fitting a smooth envelope to the total energies corresponding to a series of lattice constants.) Therefore, in Sec. IV B, relaxed energies and structures refer to structures where only intracell ionic coordinates are relaxed to their equilibrium values.

2. Finite temperature molecular dynamics

We have performed finite temperature molecular dynamics to investigate the thermal stability of some of the quenched interface structures. The initial ionic temperatures are chosen to be $T = 1600$ K within a canonical distribution. The system is kept at this temperature using a Nosé thermostat[35] with a frequency of 10.0 THz. A low electronic friction is used to maintain the electronic system close to the Born-Oppenheimer potential-energy surface. We use the simulation temperature $T = 1600$ K because it is well above the temperature for the bulk $(m \rightarrow t)$-ZrO_2 transition temperature (1450 K) and further this temperature is relevant to the environment inside a combustion engine.

The trajectory lengths are 1.4 ps, with a time step of 0.4 fs (after the electronic wave functions are relaxed to their fermionic ground state corresponding to the initial ion positions). Mass renormalization of the ions is applied, to compensate for the artificial electronic drag[23] on the ions within the Car-Parrinello formalism. The PAW CP code[23] was run in parallel on 2, 4, 8, and 16 nodes on IBM SP2 platforms.

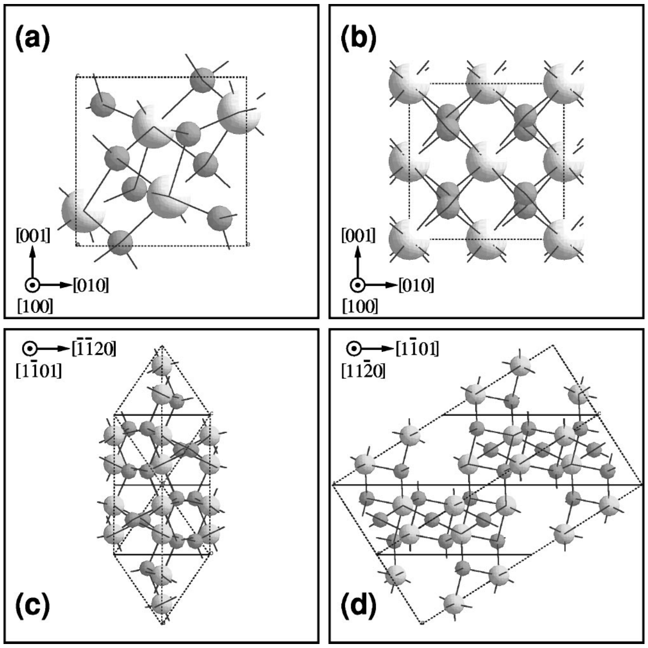

FIG. 1. Unit cells for bulk ZrO_2 and α-Al_2O_3. Oxygen ions are small and dark. Cations are larger and bright. (a) m-ZrO_2 with conventional axis assignments (i.e., $\beta > 90°$), (b) t-ZrO_2 with the tetragonal distortion along [001]. (c) and (d) The conventional hexagonal α-Al_2O_3 unit cell viewed from two angles along the $(1\bar{1}02)$ Miller planes (seen as horizontal lines in the figure from these view angles). Since only one unit cell is displayed, (d) might give the false impression of large interstitials in the crystal—this disappears, when the unit cell is repeated in all periodic directions.

III. BULK PHASES OF α-Al_2O_3 AND ZrO_2

The purpose of this section is to introduce the bulk phases of α-Al_2O_3 and ZrO_2 as well as testing our PAW method setup. Readers not interested in this may skip directly to Sec. IV. In Figs. 1(a)–1(b), we show the two low-pressure and low-temperature polymorphs of ZrO_2.[36] The most stable low-temperature structure, shown in Fig. 1 (a), has monoclinic symmetry $(P2_1/c)$ with sevenfold cation coordination, and alternating threefold and fourfold anion coordination. At intermediate temperatures (1180–2370 °C), the stable phase has tetragonal symmetry $(P4_2/nmc)$ with eightfold cation coordination and (distorted) tetrahedral anion coordination [Fig. 1(b)]. This polymorph can be made stable at room temperature in the presence of certain dopants, e.g., up to a few percent cubic oxides such as Y_2O_3. From 2370 °C to the melting temperature (2600 °C), the stable phase is fluorite, which has full cubic symmetry $(Fm\bar{3}m)$ and also eightfold cation coordination and tetrahedral anion coordination. The difference between the cubic and tetragonal structure is the small alternating distortion of the O-atom columns along the 4_2 axes [directed along [001] in Fig. 1(b)], together with a small elongation of the unit cell along

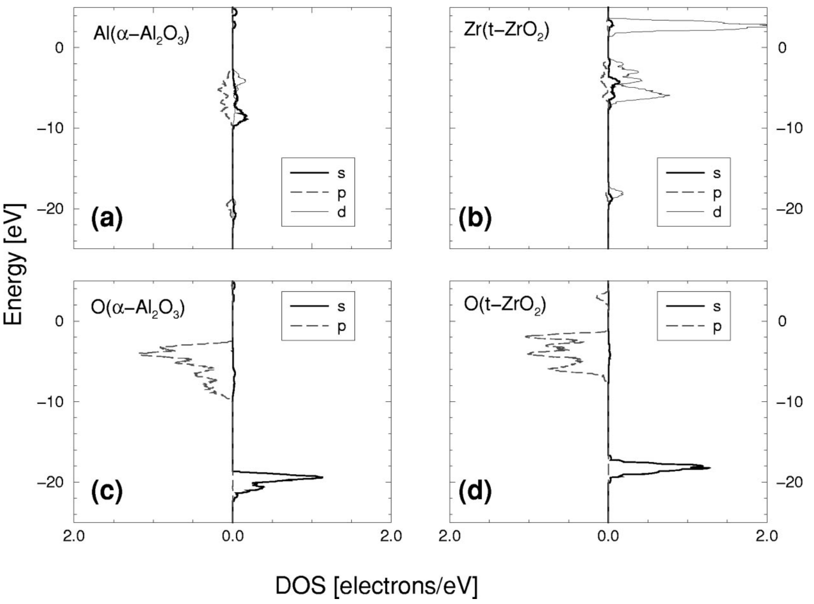

FIG. 2. Bulk density-of-states of valence electrons for α-Al_2O_3 and t-ZrO_2, projected onto anions and cations and resolved into angular momenta. The energy zero is chosen to be in the middle of the single-particle band gap. To enhance clarity in the figure, p-character DOS is plotted towards the left-hand side, whereas *s*, *d*-character DOS is plotted to the right-hand side.

the [001] direction. We will not focus on the cubic modification in this paper because it is metastable at low temperatures. For many purposes, the tetragonal phase may be considered a perturbation of the cubic phase, due to the smallness of the tetragonal distortion distinguishing it from the cubic phase. Throughout this paper, the letters *c*, *t*, and *m* refer to zirconia's cubic, tetragonal, and monoclinic phases, respectively. The bulk phases of ZrO_2 have been studied quite extensively theoretically, using DFT techniques,[37,27,38,39,14,40,15] the Hartree-Fock (HF) method,[41] tight-binding techniques,[42,43] as well as semiempirical atomistic models.[42,44]

In Fig. 1(c)–1(d), we show two views of the stable low-pressure and low-temperature polymorph of Al_2O_3, which has the corundum structure. This phase has rhombohedral symmetry ($R\overline{3}c$) and is conventionally referred to as α-Al_2O_3. In this structure, Al has sixfold coordination, whereas the O ions are tetrahedrally coordinated. Figures 1(c)-1(d) shows one single conventional hexagonal unit cell, rotated so that the view is along certain characteristic crystalline directions, parallel to the $(1\overline{1}02)$ Miller planes. The complete view of α-Al_2O_3 along the directions in Figs. 1(c)–(d) is obtained by repeating the unit cell along periodic directions [making the crystal look denser than in Fig. 1(d)]. α-Al_2O_3 will act as the substrate in our paper, therefore we consider only this polymorph.

With the calculational setup described in Sec. II, the bulk structures of ZrO_2 and α-Al_2O_3 are well reproduced. We obtain the lattice constant $a_0=5.071$ Å for c-ZrO_2, in excellent agreement with the experimental value $a_0=5.07$ Å.[36] The tetragonal distortion of the oxygen ions is found to be $|dz/z|=0.044$, in slightly better agreement with the experimental value ($|dz/z|=0.065$ at $T=1523$ K[46]) than the corresponding value $|dz/z|\sim 0.03$ (Refs. 14,27) obtained using the LDA for exchange-correlation effects. The discrepancy between theory at $T=0$ and experiment at $T=1523$ K here is primarily due to thermal volume expansion, whereby the tetragonal distortion of the oxygen ions $|dz/z|$ increases with temperature. For the monoclinic phase, we obtain $a_0=5.14$ Å, $b_0=5.25$ Å, $c_0=5.27$ Å, and $\beta=99.43°$, with ion positions generated by Zr(0.278, 0.044, 0.208), O1(0.073, 0.342, 0.338), and O2(0.449, 0.759, 0.481) from symmetry group $P2_1/c$. This compares well with the experimental structure[45] obtained by neutron powder diffraction at 295 K $a_0=5.1505$ Å, $b_0=5.2116A$ Å, $c_0=5.3137$ Å, and $\beta=99.230°$, with ion positions generated by Zr(0.2754,0.0395,0.2083), O1(0.0700, 0.3317, 0.3447), and O2(0.4496, 0.7569, 0.4792) from symmetry group $P2_1/c$. Likewise, the calculated lattice constants for α-Al_2O_3 ($a_0=4.813$ Å and $c_0=13.131$ Å) agree well with the experimentally determined $a_0=4.76$ Å and $c_0=13.00$ Å.[36] In this case all ionic degrees of freedom (including the lattice constants) are relaxed (consistent with space group $R\overline{3}c$). For the internal cell coordinates (referenced to the hexagonal cell for space group $R\overline{3}c$[47]) we obtain $z=0.3531$ for Al in Wyckoff position 12c and $x=0.3079$ for O in Wyckoff position 18e. The corresponding experimental values[36] are $z=0.352$ and $x=0.306$. The good agreement with experiment for the bulk structures lends confidence to the predictions we make below for thin films of ZrO_2 and α-Al_2O_3, albeit within the constraint that large length scale changes in structure will be excluded due to the necessary imposition of periodic boundary conditions within a tractably sized unit cell.

A. The bulk α-Al_2O_3 and ZrO_2 electronic structure

To facilitate the discussion of the electronic structure of the surfaces and interfaces of α-Al_2O_3 and ZrO_2, we briefly review the main characteristics of the bulk electronic structure of α-Al_2O_3 and t-ZrO_2 (as representative of the ZrO_2 phases). In Fig. 2, we show the one-electron energy-resolved valence DOS projected onto anions/cations and resolved into angular momenta for both α-Al_2O_3 and t-ZrO_2. For both oxides in this figure, the energy zero is chosen to be the middle of the band gap.

The classical picture of these two oxides assumes a complete charge transfer of valence electrons from metal to oxygen, thereby obtaining a closed O($2p$) shell. The O^{--} anion charge state is stabilized by the Madelung potential created by the charge transfer. From this point of view, the electronic structure of these oxides is similar to that of compressed noble gases.[48] As expected from the classical picture, the occupied anion valence DOS is larger than the cation valence DOS, but the cation DOS is significantly larger than zero, reflecting the fact that the charge transfer is incomplete. The band structures of Al_2O_3 and ZrO_2 share some characteristics: the lowest band in the valence region is derived from the $O(2s)$ state and is centered around 20 eV below the valence-band maximum. This band has a weak dispersion, with a bandwidth around 1–2 eV, indicating the $O(2s)$ electrons are very localized. The valence band is derived from the $O(2p)$ state and shows a larger dispersion than the $O(2s)$ band, indicating significant delocalization. Both the $O(2s)$ and $O(2p)$ bands are broader for Al_2O_3 than for ZrO_2. The conduction bands are derived from the empty cation valence states, with the bottom of the conduction bands being mainly *s*-like for Al_2O_3 and mainly *d*-like for ZrO_2.

Generally, covalent interactions are visible in the DOS spectrum as a simultaneous down and up shift of occupied and unoccupied states, respectively, and mixing of electronic states of the interacting elements. Conduction-band valence-band interactions give rise to stabilizing covalent effects for these oxides, the nature of which is revealed in the cation projections of the $O(2p)$ derived band. These covalent interactions, considered alone, increase the intrinsic single-particle band gap in these oxides. Valence-valence interactions between the oxygens are mainly nonbonding and dispersive, because the valence states are completely filled; these tend to decrease the band gap by pushing up the valence-band maximum. Al_2O_3 has a larger intrinsic ionicity and band gap, due to a larger intrinsic separation of the Al(3s) and O(2p) resonances in the ionic crystal leading to a more complete charge transfer for Al_2O_3.

Comparing Figs. 2(a) and 2(b) suggests that ZrO_2 is more covalent than Al_2O_3, due to the relatively larger weight of the valence bands on Zr ions compared to Al ions. Thus Zr is likely to be more Zr(II)-like, which is consistent with the fact that it is typically easy to strip $Zr(5s)$ electrons off the Zr atoms, while the ionization potential for the $Zr(4d)$ electrons is considerably higher.[49]

Although it is not formally correct to associate the eigenvalue band gap in DFT with the experimental optical band,[50] comparison is frequently made. Generally, the calculated eigenvalue band gaps are smaller than the corresponding experimental optical band gaps for the LDA and GGA. For m-ZrO_2, the calculated (direct) band gap is 3.6 eV, to be compared with the experimental optical band gap around 5 eV.[51] For α-Al_2O_3, the calculated band gap (direct) is 5.8 eV, considerably lower than the accepted experimental value of 8.7 eV.[52]

B. Origin of phase stability in ZrO_2

Since the energy differences between competing ZrO_2 bulk phases are relatively small, and the corresponding unit cells have different shapes, we increased the kinetic-energy cutoff to 55 Ry (749 eV) for the plane-wave basis, to achieve absolute convergence of total energies reported in this section. This is feasible, because the bulk unit cells are much smaller than the interface unit cells in Sec. IV B.

Our PAW calculations suggest that the structural energy difference $\Delta E^{t-c}=E^{t}-E^{c}$ between t-ZrO_2 and c-ZrO_2 is -0.038 eV/ion, in favor of t-ZrO_2, in agreement with the experimental phase ordering. The fact that the PAW method is an all-electron formalism allows direct decomposition of the structural energies into native DFT components:

$$\Delta E^{t-c}=\Delta E^{t-c}_{\text{kinetic}}+\Delta E^{t-c}_{\text{electrostatic}}+\Delta E^{t-c}_{\text{exchange}-\text{correlation}}. \tag{1}$$

This yields $\Delta E^{t-c}_{\text{kinetic}}=0.912$ eV/ion, $\Delta E^{t-c}_{\text{electrostatic}}=-0.924$ eV/ion, and $\Delta E^{t-c}_{\text{exchange}-\text{correlation}}=-0.025$ eV/ion, so that $(c\rightarrow t)$ transition is driven by electrostatics. Given that the one-electron kinetic-energy and classical electrostatic terms cancel each other nearly exactly, a major part of the net stabilization of t-ZrO_2 is derived from the nonclassical exchange-correlation term. This is not surprising, since the $(c\rightarrow t)$ transition has character of an anion-cation bond stretching, where correlation is expected to play an important role. For the t-ZrO_2 and m-ZrO_2, our PAW calculations suggest that the structural energy difference ΔE^{m-t} is -0.063 eV/ion, in favor of m-ZrO_2, also in agreement with the experimental observed phase ordering. Decomposing this structural energy into native DFT components gives $\Delta E^{m-t}_{\text{kinetic}}=-0.733$ eV/ion, $\Delta E^{m-t}_{\text{electrostatic}}=0.370$ eV/ion, and $\Delta E^{m-t}_{\text{exchange}-\text{correlation}}=0.300$ eV/ion, so that the $(t\rightarrow m)$ transition is driven by kinetic-energy lowering. This is understandable because the $(t\rightarrow m)$ transition is accompanied by a significant volume expansion of 4%, and the kinetic-energy term is stabilizing when expanding a solid (further electron delocalization). The experimental value[53] for ΔE^{m-t} is -0.02 eV/ion, so that the structural energy difference between m-ZrO_2 and t-ZrO_2 is overestimated somewhat. This is a consequence of the GGA for exchange-correlation effects, and this effect has also been noted previously for ZrO_2 by Jomard *et al.*[40] For this physical quantity, the LDA seems to give a result[14] in better agreement with experiments: $\Delta E^{m-t}=-0.026$ eV/ion. The apparent overestimation of ΔE^{m-t} is a consequence of using a GGA, not the omission of Zr semicore states from the valence; we tested this issue, using the pseudopotential code VASP (Vienna *ab initio* simulation program).[54] Here we find that the structural energy ΔE^{m-t} obtained with a GGA (Ref. 55) is decreased by 2% when including the $Zr(4p)$ semicore states. Generally for ZrO_2, we expect the effect of Zr semicore states to be less than the sensitivity of which particular GGA parametrization is applied.[13]

IV. SURFACES AND INTERFACES OF α-Al_2O_3 AND ZrO_2

In Sec. IV A we start by investigating the geometrical aspects of forming an interface between α-Al_2O_3 and ZrO_2 crystals from a very general point of view. This investigation attracts our attention to two particular surfaces of α-Al_2O_3 and ZrO_2, which should form a stable interface from an elasticity point of view. This particular choice of surfaces is also supported by experiments. Then in Sec. IV B we investigate the properties of these particular ceramic surfaces, we discuss m-t phase stability in ZrO_2 films in Sec. IV C and finally in Secs. IV D–IV H, we analyze the interface formed by these ceramic surfaces.

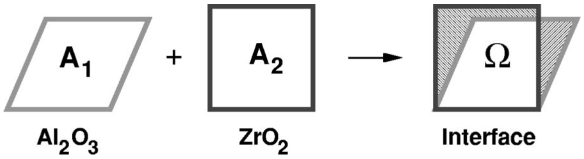

FIG. 3. Sketch of a surface unit cell of α-Al_2O_3 with area A_1 and a surface unit cell of ZrO_2 with area A_2. Both unit cells may be multiples of a primitive surface unit cell, so that they contain several equivalent lattice points. Ω is the overlap area between the cells when overlaid.

TABLE I. Best matching unit cells, according to the misfit measure μ defined in Eq. (2), of different α-Al_2O_3 and c-ZrO_2 surfaces (restricted to surface areas less than 50 Å^2).

Faces		Unit-cell	Misfit	Experiments
α-Al_2O_3	c-ZrO_2	area (Å^2)	(μ)	
$1\bar{1}02$	001	24.4	0.037	Refs. 16 and 17
0001	001	39.2	0.095	Ref. 20
0001	110	39.2	0.042	
$11\bar{2}0$	110	35.7	0.017	
$11\bar{2}0$	110	35.7	0.028	

A. Interface geometry

We are considering the situation where ZrO_2 is deposited on top of a crystalline α-Al_2O_3 surface. The structural possibilities for constructing a ZrO_2/α-Al_2O_3 interface are immense. First, there is the choice of which stable crystal surface of each ceramic to match against each other and how each should be oriented relative to each other. Then there is the question about termination and stoichiometry of both the ZrO_2 and Al_2O_3 sides of the interface. Finally, there is the issue of how the ZrO_2 and Al_2O_3 crystals will lock-in to each other. The latter generally requires atomistic simulations. Nature allows for aperiodicity at the interface, but our computational method relies on periodic boundary conditions, so it is necessary to enforce some degree of interface coherency, which translates into a choice of a unit cell for the interface. Of course, if the unit cell is sufficiently large, an aperiodic interface can be modeled, but this is currently far out of reach of *ab initio* methods. Educated guesses are necessary here. The key objective is the matching of lattice vectors in the interface plane of each ceramic, so that the overall strain is small, when the interface is formed. Many related approaches may be used to achieve this, but we will apply a rather simple geometrical principle, which is illustrated in Fig. 3. Some surface unit cell of ZrO_2 with area A_2 is forced into coherency with a substrate (α-Al_2O_3) surface unit cell with area A_1. By overlaying these unit cells, as indicated on the right-hand side of Fig. 3, we calculate the overlap area Ω. We then define a misfit μ as

$$\mu = 1 - \frac{2\Omega}{A_1 + A_2}. \tag{2}$$

The measure μ is positive definite and quantifies the relative average length scale misfit (and not area mismatch) between two unit cells, which is seen by first-order expansion in the shape difference between two unit cells. In Table I we show the best matching unit-cell pairs, according to their μ value, for cells with area less than 50 Å^2. For simplicity and to compare with experiments, we use the c-ZrO_2 lattice in this scanning process. Because the lattice constants of the ZrO_2 polymorphs differ by only a few percent, the matches in Table I also apply to the other ZrO_2 polymorphs as well. However, one has to take into account all inequivalent lattice directions that correspond to each high-symmetry direction in c-ZrO_2. We exclude some very elongated unit cells, which are rather unrealistic as interface unit cells. As seen from this table, the c-$ZrO_2(001)||\alpha$-$Al_2O_3(1\bar{1}02)$ combination has an acceptably low misfit μ of 4%. Moreover, this unit cell is orthogonal, and manageably small, 4.76 Å $\times$5.13 Å. The corresponding directions of the interface basis vectors are $[11\bar{2}0]$ and $[\bar{1}10\bar{1}]$. Experimentally, the growth direction of deposited YSZ has been observed as α-$Al_2O_3(1\bar{1}02)||$YSZ(001)[16,17] at medium temperatures ($<820\,°C$). (YSZ has a quasicubic structure, with roughly the same lattice constant as c-$ZrO_2(001)$, but no information on the interface unit-cell size is available.) We focus on the $ZrO_2(001)||\alpha$-$Al_2O_3(1\bar{1}02)$ interface in the present paper. The $(1\bar{1}02)$ surface is often referred to as the *R* plane in the literature.

When searching for the most stable interface matching of two crystalline materials, it is generally not enough to consider the unit-cell combination with lowest strain. The chemical component of interface cohesive energy, defined as the remainder after the elastic part has subtracted, may be rather irregular for different interface cell combinations, because of atomic level corrugation and bonding. The possibility of competition exists and may result in a medium-strained interface being more stable than a low-strained interface.

We have studied the ZrO_2/α-Al_2O_3 interface using a slab geometry and the unit-cell match corresponding to the first entry in Table I. We choose the α-Al_2O_3 substrate to be 10.5 Å thick, corresponding to three α-$Al_2O_3(1\bar{1}02)$ layers. This substrate thickness is usually enough to emulate a bulk ceramic surface, both with regard to electronic structure and ionic relaxation effects.[14] We will validate this assertion in Secs. IV D, IV E, and IV G.

A side view of the interface structures studied in our paper is shown in Figs. 4(a)–4(c). Each $ZrO_2(001)$ overlayer is approximately 3 Å thick. Our geometry corresponds physically to an infinite array of ZrO_2/α-Al_2O_3 thin-film couples, with vacuum between them. We use 10 Å vacuum in between the thin-film couples, which is usually enough to ensure negligible coupling between the thin-film couples,[14] unless a large dipole is present at the interface.

Figure 4 also displays the crystal termination of each ceramic that we use in our paper. For α-$Al_2O_3(1\bar{1}02)$ the choice indicated in this figure is quite natural in that it follows the layering appearance of the crystal, when the view direction is parallel to the surface. The layering sequence in this surface termination is |O-Al-O-Al-O|O-Al-O-Al-O| . . . . This results in a compact surface, see Fig. 1(d) [note that the unit cell shown in Fig. 1(d) does not encapsulate the α-$Al_2O_3(1\bar{1}20)$ crystal-

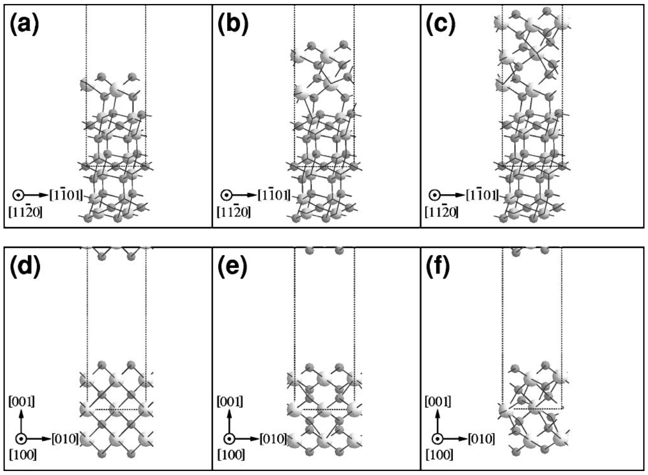

FIG. 4. Lowest-energy structures $ZrO_2(001)/\alpha\text{-}Al_2O_3(1\bar{1}02)$ interface structures (a)–(c). Oxygen ions are drawn small and dark, Al ions medium sized and light gray, Zr ions largest and brightest. In (a)–(c), the Al_2O_3 substrate has three layers, corresponding to a thickness of 10.5 Å. The directional arrows in (a)–(c) refer to the $\alpha\text{-}Al_2O_3$ substrate lattice. One ZrO_2 overlayer corresponds to approximately 2.9 Å. (a) One layer ZrO_2 deposited, (b) two layers ZrO_2 deposited, (c) three layers ZrO_2 deposited. (d)–(f) $ZrO_2(001)$ surface slabs for the *c*, *t*, and *m* phase of ZrO_2, each with three layers. (d) $c\text{-}ZrO_2$; if ions are relaxed, $c\text{-}ZrO_2(001)$ transforms into $t\text{-}ZrO_2(001)$. (e) $t\text{-}ZrO_2$, ions relaxed. (f) $m\text{-}ZrO_2$, ions relaxed.

line substrate displayed in Fig. 4]. The lowest-energy surfaces tend to be compact, also for ionic materials.[14] Placing the $(1\bar{1}02)$ cleavage plane at any other altitude will result in more broken anion-cation bonds. In a study of the $\alpha\text{-}Al_2O_3(1\bar{1}02)$ surface using the self-consistent field discrete variational method (SCF-DV), Guo *et al.*[56] considered alternative cleavage planes than the one implied in Fig. 1(d)—all were found to have significantly higher cleavage energy. Further, our chosen surface termination is stoichiometric.

The termination of $c\text{-}ZrO_2(001)$ is more debatable: the layering sequence for $c\text{-}ZrO_2(001)$ is $\mathrm{Zr}\,|\,2\mathrm{O}|\mathrm{Zr}|2\mathrm{O}|\mathrm{Zr}|2\mathrm{O}\ldots$ viewed from the angle in Fig. 4(d), where half the oxygen ions reside behind the front oxygen ions. (Zr ions at unit-cell boundaries should only be counted once.) Letting the $c\text{-}ZrO_2(001)$ relax perpendicular to the surface transforms the structure into $t\text{-}ZrO_2(001)$, with the tetragonal distortion perpendicular to the surface, which is seen in Fig. 4(e). This ionic relaxation lowers the energy significantly[14] and splits the oxygen layers so that the oxygen ions becomes associated to a Zr plane. It is therefore natural to view the stacking sequence as $|\mathrm{O\text{-}Zr\text{-}O}|\mathrm{O\text{-}Zr\text{-}O}|\mathrm{O\text{-}Zr\text{-}O}|\ldots$ whereby the layers become stoichiometric. It is important to layer-associate the oxygen ions in accordance with the tetragonal distortion, so that oxygen ions can relax inwards on both sides of the slab, otherwise the surface energy of the structure increases significantly. In this way, the $ZrO_2(001)$ surface becomes semiterminated with oxygen, stoichiometric and nonpolar. Polar ceramic surfaces are notoriously unstable.[57]

TABLE II. DFT-GGA surface energies for $\alpha\text{-}Al_2O_3(1\bar{1}02)$ and $t\text{-}ZrO_2(001)$ (ions relaxed; equilibrium bulk lattice constants).

Layers	Surface energy (mJ/m^2)	
	$\alpha\text{-}Al_2O_3(1\bar{1}02)$	$t\text{-}ZrO_2(001)$
1		675
2		757
3	1055	803
4	1014	785

B. The clean $\alpha\text{-}Al_2O_3(1\bar{1}02)$ and $ZrO_2(001)$ surfaces

In Table II we show the surface energies of $\alpha\text{-}Al_2O_3(1\bar{1}02)$ and $t\text{-}ZrO_2(001)$ after an ionic relaxation is performed. Allowing for ionic relaxation, a $c\text{-}ZrO_2$ slab transforms into a $t\text{-}ZrO_2$ slab by a barrierless transition, even when the unit-cell dimensions are frozen. For the $t\text{-}ZrO_2(001)$ surface, the tetragonal distortion is oriented along the surface normal, as seen in Fig. 4(e), which reduces the surface energy significantly.[14] The results in Table II refer to the case where the surface unit-cell lattice vectors are fixed to their respective bulk value. The surface energy converges fast with slab thickness, as is also the case for transition-metal surfaces. A nearsightedness principle is also valid for these ceramic surfaces, as discussed by Christensen and Carter,[14] due to the localized and inert nature of the electronic structure. In Table II we observe an oscillation in the surface energy for $t\text{-}ZrO_2$, apparently depending on the $t\text{-}ZrO_2$ slabs being odd layered/even layered. This may be related to the fact that odd-layered crystalline $t\text{-}ZrO_2(001)$ slabs have symmetry $P\bar{4}m2$, whereas even-layered crystalline $t\text{-}ZrO_2(001)$ slabs have symmetry $Pmmn$. When forming the ZrO_2/Al_2O_3 onto Al_2O_3, ZrO_2 becomes slightly strained to accommodate the 4% mismatch. In Sec. IV F we return to this issue.

We observe a dramatic lowering (by more than a factor of 2) of the surface energy of $t\text{-}ZrO_2(001)$ when applying the GGA instead of the LDA. The latter yields a surface energy of 1577 mJ/m^2, (Ref. 14) similar to predictions from periodic Hartree-Fock calculations of a surface energy of 1630 mJ/m^2 for a three layer slab.[58] A similar effect has been found by applying the GGA to the $TiO_2(110)$ and $SnO_2(110)$ surfaces.[59,60] In contrast, Guo *et al.*,[56] using the SCF-DV embedded cluster method for $\alpha\text{-}Al_2O_3$ surfaces, found only very small changes by applying a GGA; for the $\alpha\text{-}Al_2O_3(1\bar{1}02)$ surface they found a surface energy of 2950 mJ/m^2 (ions unrelaxed), which is in quantitative disagreement with our all-electron calculations, which yield 1702 mJ/m^2 for a three layer slab with unrelaxed ions. One might speculate that the source of the discrepancies are the boundary conditions introduced by the embedding method used by these authors. Manassidis and Gillan[61] studied five low index $\alpha\text{-}Al_2O_3$ surfaces with the LDA and the pseudopotential formalism and found relaxed surface energies in the range 1400–2550 mJ/m^2, further supporting the trend of the GGA dramatically lowering the surface energies of oxides. Hartree-Fock calculations[62] also yield very large values of surface energies for relaxed low index $\alpha\text{-}Al_2O_3$ surfaces, of order 5000 mJ/m^2.

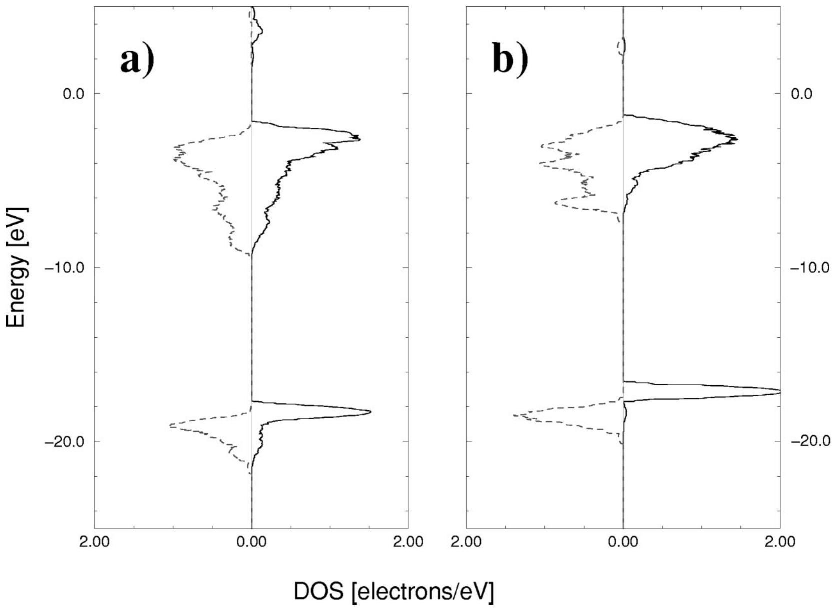

FIG. 5. The valence DOS for surface anions compared to bulk anions. (a) α-$Al_2O_3(1\bar{1}02)$ and (b) t-$ZrO_2(001)$ (unstrained unit cell). In each graph box, the solid line shows a surface anion and the dashed line is a corresponding bulk anion. The bulk anion DOS is plotted to the left.

In conclusion, a tendency for smaller surface energies when using the GGA instead of the LDA is clear. Comparison with experiments suggest that the GGA results are closer to reality than LDA or Hartree-Fock results for surface energies; the surface free energies of typical metal oxides fall in range 300–900 mJ/m^2.[63] Virtually all *ab initio* calculations refer to $T=0$ K, so an entropy correction of order 0.4 mJ/m^2 must be included for a proper comparison,[64] but still the GGA results are closer to reality than LDA results for surface energies. This is not particularly surprising, since it is well known that both the LDA and the HF methods will overestimate the energy to break bonds. Since the energy to form a surface involves exactly this process (bulk bond breaking), it is to be expected that the GGA would improve greatly upon the overestimates from the other two theories.

In Figs. 5(a) and 5(b) we show the DOS of surface anions (solid lines) for α-$Al_2O_3(1\bar{1}02)$ and t-$ZrO_2(001)$, respectively, compared to a corresponding bulk anion in each oxide (dashed lines). The DOS for t-$ZrO_2(001)$ corresponds to the unstrained unit cell. The surface ions are relaxed in both cases. For both oxides, a surface band narrowing is visible, due to decreased coordination, and localization of electronic charge as for covalent surfaces. A corresponding upshift of all electronic states at the surface due to the decreased surface Madelung potential is also clear. Further, the characteristic Zr(d) features in the t-ZrO_2 valence band is smoothed at the surface, indicating again the decreased coordination at the surface, which decreases the crystal-field splittings of the bands [compare to Fig. 2(b) which shows that the t-ZrO_2 valence-band character has strong Zr(d) character].

C. The monoclinic-tetragonal phase transition in thin $ZrO_2(001)$ films

Since the stable low-temperature phase of zirconia is m-ZrO_2, t-ZrO_2 slabs will eventually transform into m-ZrO_2 at low temperatures, if the slabs are sufficiently thick. An interesting question is if there exists an ultrathin-film regime, where t-ZrO_2 is actually more stable than the corresponding m-ZrO_2 thin film at low temperatures. Experimentally, thin t-ZrO_2 films have been stabilized in dense sandwich structures with amorphous alumina.[22] For the bulk $(t\rightarrow m)$ transition an orientational relationship exists[65] between crystalline directions in the (t,m) phases. This relationship implies that the t-$ZrO_2(001)$ transforms into the m-$ZrO_2(001)$ surface. Our previous work[14] suggests that the surface energy for the m-$ZrO_2(001)$ surface is $\sim$200 mJ/m^2 higher than for t-$ZrO_2(001)$. Since the bulk $(t\rightarrow m)$ transformation energy obtained in our calculations is ~ -0.06 eV/ion, a back-of-the-envelope estimate suggests that only a few layers of t-$ZrO_2(001)$ may be stable at low temperatures. However, the m phase is not rigorously distinguishable from the t phase for very thin films; establishing the characteristic sevenfold Zr-cation coordination requires at least three $ZrO_2(001)$ layers. On the other hand, the pinning provided by the substrate might increase the absolute stability regime of t-$ZrO_2(001)$ at low temperatures, due to the significant volume increase of 4% for the bulk t-$\rightarrow m$-ZrO_2 transition.

Table III shows the transformation energy, normalized per unit area, between isolated t-$ZrO_2(001)$ and m-$ZrO_2(001)$ slabs for different numbers of ZrO_2 layers. The unit cell is fixed to the dimensions given by the lock-in to the α-$Al_2O_3(1\bar{1}02)$ substrate, which corresponds to a $\sim$4% lattice mismatch, as discussed in Sec. IV A. In all three cases, the slab structure relaxes to a structure appearing like the m-$ZrO_2(001)$; see Fig. 6 (upper row) and compare to the bulk unit cell in Fig. 1(a). Thus the t-$ZrO_2(001)$ slabs, see Fig. 6 (lower row), are only locally stable. Strictly speaking, as mentioned above, it only makes sense to talk about the

TABLE III. Energy gain per unit area by $(t\rightarrow m)$ transformation for ultrathin $ZrO_2(001)$ slabs.

ZrO_2 layers	$t\rightarrow m$ energy (mJ/m^2)
1	21
2	55
3	96

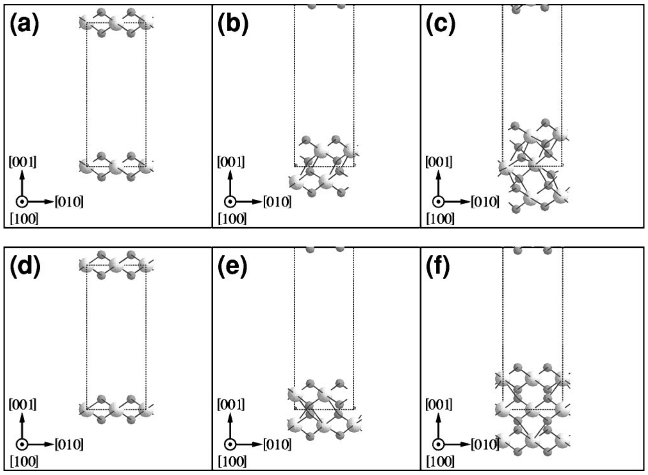

FIG. 6. The incomplete t-$ZrO_2 \rightarrow m$-ZrO_2 transition in 4% compressed thin $ZrO_2(001)$ slabs. Oxygen ions are small and dark, whereas Zr ions are larger and brighter. In all cases (a)–(f) the surface lattice vectors are pinned to the α-$Al_2O_3(1\bar{1}02)$ substrate with the lock-in discussed in Sec. IV A. (a)–(c) One-, two-, and three-layer $ZrO_2(001)$ slabs after the incomplete t-$ZrO_2 \rightarrow m$-ZrO_2 transition. (d)–(f) Comparison for one, two, and three layers of t-$ZrO_2(001)$, which correspond to local minima in the total energy. (a)–(c) should be compared with Fig. 1(a).

monoclinic structure for 3 or more layers of ZrO_2, but from Fig. 6 it seems that the one- and two-layer $ZrO_2(001)$ slabs transform into a precursor of m-$ZrO_2(001)$. The transition is incomplete, though, as revealed by the coordination around the middle layer cations in Fig. 6(c), which have anion-cation bond lengths of (1.98, 2.04, 2.04, 2.08, 2.20, 2.38, 2.38) Å and (1.98, 2.02, 2.04, 2.06, 2.20, 2.38, 2.42) Å, respectively. There are two sets of bond lengths, because the symmetry is broken and the two middle cations are inequivalent. The corresponding m-ZrO_2 bulk anion-cation bond lengths are (2.06, 2.06, 2.14, 2.16, 2.16, 2.22, 2.26) Å. This incomplete transition is mainly related to the fact that we froze the surface lattice vectors to those in registry with the α-$Al_2O_3(1\bar{1}02)$ substrate. Despite this confinement, the t-ZrO_2 slabs transform into a structure close to m-ZrO_2. Furthermore, this transition is in accord with the direction relation established by Bansil and Heuer,[65] i.e., t-$ZrO_2(001)||m$-$ZrO_2(001)$, as is apparent when comparing Fig. 6 and Figs. 1(a) and 1(b).

It is unlikely that the t-$\rightarrow m$-ZrO_2 transition we find in ultrathin ZrO_2 films is strain induced, because the straining necessary to obtain lock-in with the α-$Al_2O_3(1\bar{1}02)$ substrate actually corresponds to a 3% volume *decrease* of the t-ZrO_2 crystal, whereas the t-$\rightarrow m$-ZrO_2 transition is accompanied by a 4% volume *increase*. Thus, if anything, the α-$Al_2O_3(1\bar{1}02)$ substrate should inhibit the $t \rightarrow m$ transition, and yet we observe it to occur.

D. Interface structure

In this section we address the structural properties in the interface region of $ZrO_2(001)/\alpha$-$Al_2O_3(1\bar{1}02)$. ZrO_2 in the c phase is deposited onto Al_2O_3 as thin films and the structure is subsequently relaxed. This procedure is meant to mimic plasma spraying or another process leading to granular microstructure, but is not meant to represent an atomic growth mechanism, like vapor deposition. Such processes are next to impossible to simulate on the *ab initio* level, due to the long-time scales involved in diffusion, but also the additional complexity introduced by needing to consider chemical potentials, which may give rise to nonstoichiometry in the interface region.

In Fig. 4 we show the lowest-energy quenched interface structures we find for one, two, and three deposited ZrO_2 overlayers, juxtaposed with a three-layer (001) slab of each ZrO_2 phase, *c*, *t*, and *m*. These ZrO_2 overlayers are deposited onto a three-layer α-$Al_2O_3(1\bar{1}02)$ substrate, corresponding to a thickness of 10.5 Å, which emulates the macroscopic α-$Al_2O_3(1\bar{1}02)$ substrate. We will return to the issue of finite substrate thickness later.

The interface structure with two ZrO_2 overlayers [Fig. 4(b)] seems to have the ZrO_2 overlayers translated with respect to the Al_2O_3 substrate. However, the two $Al_2O_3(1\bar{1}02)$ surface anions in the unit cell are symmetry equivalent, so that the ZrO_2 film has simply been locked into the substrate at a different, but equivalent point.

The general impression is that the α-$Al_2O_3(1\bar{1}02)$ substrate maintains its crystallinity more than the ZrO_2 adlayers, which appears more glassy. This is especially the case for the anion lattice on the ZrO_2 side of the interface. Also, the Zr layers close to the interface buckle more than Zr layers farther from the interface as seen in Figs. 4(b) and 4(c). The fact that the ZrO_2 adlayers seem to become most perturbed from crystallinity is understandable considering the fact that ZrO_2 is forced into registry with the substrate and further that bulk α-Al_2O_3 has a stiffness twice that of bulk ZrO_2.

We performed molecular-dynamics sequences at $T = 1600$ K for the interface structures with one- and two- layered ZrO_2 films to explore the stability of the quenched structures. In both cases, at high temperatures, there are cation-cation interactions at the interface, between cations closest to the interface. When we requench the structures, the cation-cation interaction disappears for the monolayer ZrO_2 film, because the Zr dives back into the ZrO_2 film and we reobtain the original low-temperature structure. However, for the bilayered ZrO_2 film, the cation-cation interaction remains stable after requench. We show this structure in Fig. 7(b), along with the structure we obtain by just depositing a two-layered ZrO_2 film and quenching the structure in Fig. 7(a)—this structure corresponds to a local minimum in the total energy. Figure 7(b) is 0.09 eV/unit cell lower in energy than Fig. 7(a). The shortest Al/Zr distances across the interface for the structures in Fig. 7 are 3.03 Å and 2.85 Å for Figs. 7(a) and 7(b), respectively. For comparison, the smallest bulk cation-cation bond lengths are $d(\text{Zr-Zr}) = 3.34$ Å in m-ZrO_2 and $d(\text{Al-Al}) = 2.68$ Å in α-Al_2O_3. The simple average of these bulk values is $d(\text{Al-Zr}) = 3.01$, relatively close to most values in Table IV, but 0.16 Å longer than for the interface structure displayed in Fig. 7(b). [In Table IV, 2a and 2b refers to Figs. 7(a) and 7(b), respectively.] We also see that this recoordination of the Zr ion closest to the interface generally induces some distortion in the anion lattice in the three-layer ZrO_2 film. We will discuss how this affects the electronic density of states in Sec. IV H.

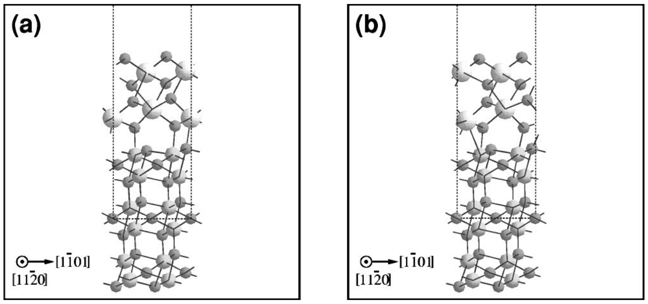

FIG. 7. Two minima for α-$Al_2O_3(1\bar{1}02)$ + two layers $ZrO_2(001)$. Oxygen ions are drawn small and dark, Al ions medium-sized and light gray, Zr ions largest and brightest. (a) is obtained by deposition of c-ZrO_2 and just quenching the structure. (b) is obtained by heating (a) to $T=1600$ K and requenching the structure. (b) is identical to Fig. 4(b). (b) is 0.09 eV/unit cell more stable than (a). The shortest Al-Zr distances across the interface for the structures in (a) are 3.03 Å and 2.85 Å in (b). For comparison, the smallest bulk cation/cation bond lengths are $d(\text{Zr-Zr}) = 3.34$ Å in m-ZrO_2 and $d(\text{Al-Al}) = 2.68$ Å in α-Al_2O_3.

It is clear from Figs. 4(a)–4(c), compared to Fig. 4(d)–4(f) that the m phase of the ZrO_2 overlayers are also energetically preferred, when the interface to α-$Al_2O_3(1\bar{1}02)$ is formed. Table IV shows the ionic bond lengths in the interface region, divided according to whether the bonds are across or mostly parallel to the interface, i.e., within the surfaces of each oxide forming the interface. No systematic trend is apparent with the variation in number of ZrO_2 layers. Bonds across the interface are typically close to the shortest value in the bulk crystal [1.88 Å for α-Al_2O_3, 2.06 and 2.09 for (m,t)-ZrO_2, respectively]. Parallel to the interface, a range of bond lengths is observed. On the Al_2O_3 side, these ranges are mostly delimited by the bulk values (1.88 and 1.99 Å), whereas on the ZrO_2 side, bond lengths are shorter than the smallest bulk values. Comparing results for a ZrO_2 monolayer deposited onto three and four layers of α-$Al_2O_3(1\bar{1}02)$, respectively, suggests that also interface structural properties are well converged with respect to substrate thickness at three layers of alumina.

Figure 4(b)–4(c) shows that both α-$Al_2O_3(1\bar{1}02)$ and $ZrO_2(001)$ have four anion-cation bonds between each layer per unit cell in the bulk part. However, there are only three anion-cation bonds across interface [except for the bilayer ZrO_2 film, where some (screened) cation-cation interaction is found, adding stability to this structure]. One Al_2O_3-side oxygen ion is unsaturated (does not coordinate with a Zr ion), partly due to a Zr-layer buckling normal to the interface, but also an intrinsic symmetry mismatch for the interface combination $ZrO_2(001)||\alpha$-$Al_2O_3(1\bar{1}02)$; although the crystalline length scales fit very well, the anion-cation alignment across the interface is not ideal. Such a situation of interface structural frustration is also expected for other heterogeneous interfaces. This nonideal alignment of anion-cation pairs across the interface partly explains the weak $ZrO_2(001)||\alpha$-$Al_2O_3(1\bar{1}02)$ cohesion, discussed in the next section.

E. Interface cohesion

In this section we focus on the energetic aspects of the ZrO_2/Al_2O_3 interface. The main quantity is the adiabatic work of adhesion $W>0$:

$$W = E_{Al_2O_3} + E_{ZrO_2} - E_{ZrO_2||Al_2O_3}, \tag{3}$$

where $E_{Al_2O_3}$,E_{ZrO_2}, and $E_{ZrO_2||Al_2O_3}$ refer to the total energies of the relaxed, isolated Al_2O_3 and ZrO_2 films and $E_{ZrO_2||Al_2O_3}$ refers to the total energy of the relaxed interface structure. Generally, the mechanical work needed to separate an interface is larger than the adiabatic work of adhesion W due to dissipative processes, as discussed by Finnis.[48] Thus our predictions may be considered as rough lower bounds for the work of adhesion obtained by any cleavage experiment.

In Table V we show the calculated adiabatic work of adhesion W for α-$Al_2O_3(1\bar{1}02)$ with various numbers of $ZrO_2(001)$ layers deposited and the interface subsequently relaxed. In Eq. (3), E_{ZrO_2} refers to the energy of the isolated, relaxed $ZrO_2(001)$ slabs subject to the *same* periodic boundary conditions as in the interface calculation that produces $E_{ZrO_2||Al_2O_3}$, i.e., in the incomplete monoclinic phase, as discussed in Sec. -IV C. It is important to subtract this quantity from $E_{ZrO_2||Al_2O_3}$ and not the energy of an m-$ZrO_2(001)$ slab with bulk m-ZrO_2 lattice constants, because then the value obtained for W contains a bulk plastic component, which diverges with increasing numbers of ZrO_2 layers deposited. Moreover, this bulk strain component is unrelated to the local cohesive properties of the interface *per se*, which we

TABLE IV. Bond lengths (Å) in the $ZrO_2/Al_2O_3(1\bar{1}02)$ interface region. [ ] = indicates a range of bond lengths are present.

Ceramic layers in slab		Direction of bonds with respect to interface: Across			Parallel	
Al_2O_3	ZrO_2	Al-O	Zr-O	Al-Zr	Al-O	Zr-O
3	1	1.91	2.12	3.02,3.09	[1.83–2.00]	[1.94–2.10]
3	2a[a]	1.88,1.94	2.07	3.03,3.08	[1.82–2.00]	[1.98–2.10]
3	2b[b]	1.86,1.87	2.13	2.85,4.19	[1.84–2.02]	[2.01–2.09]
3	3	1.85,1.87	2.09	2.98,3.05	[1.85–2.02]	[1.96–2.09]
4	1	1.90,1.91	2.12	3.01,3.11	[1.83–2.00]	[1.94–2.09]

[a] Two layers of ZrO_2, with structure corresponding to Fig. 7(a). See Sec. IV D for more details.

[b] Two layers of ZrO_2, with structure corresponding to Fig. 7(b). See Sec. IV D for more details.

TABLE V. DFT-GGA adiabatic adhesion energies W for the $ZrO_2(001)/\alpha\text{-}Al_2O_3(1\bar{1}02)$ interface.

Number of oxide layers		W
Al_2O_3	ZrO_2	(mJ/m^2)
3	1	1142
3	2[a]	1201
3	2[b]	1256
3	3	1189
4	1	1143

[a] Two layers of ZrO_2, with structure corresponding to Fig. 7(a). See Sec. IV D for more details.

[b] Two layers of ZrO_2, with structure corresponding to Fig. 7(b). See Sec. IV D for more details.

want to characterize. Of course, this means in principle that one has to subtract an accommodation energy for the ZrO_2 adlayers from our value of W to obtain an ‘‘experimental’’ value. This accommodation energy will represent dislocations and other defects possibly created on the ZrO_2 side on intermediate length scales.

It is seen that W has values $\sim$1200 mJ/m^2 and that there is no systematic variation with the number of layers—in other words, the chemistry of the ZrO_2/Al_2O_3 is rather local and defined by the ZrO_2 layer closest to the interface. This is not obvious *a priori*, due to the long-ranged electrostatic interactions present in ionic materials. It is also clear, comparing the results for one layer of ZrO_2 deposited onto three and four layers of $\alpha\text{-}Al_2O_3(1\bar{1}02)$, respectively, that energetic properties are very well converged with respect to substrate thickness. Counting three anion-cation bonds across the interface per unit cell gives an average bond energy of 0.6 eV/bond, i.e., in the weak chemical bonding regime. For comparison, the corresponding cleavage energies for the bulk oxides are 0.63 eV/bond and 0.79 eV/bond for $t\text{-}ZrO_2(001)$ and $\alpha\text{-}Al_2O_3(1\bar{1}02)$, respectively (relaxation effects included), so that ZrO_2/Al_2O_3 bonds are slightly weaker than the constituent bulk oxide bonds. This fact is also expressed quantitatively, normalized by interface area, in the interface tension $\sigma_{ZrO_2||Al_2O_3}$:

$$\sigma_{ZrO_2||Al_2O_3}=\sigma_{Al_2O_3}+\sigma_{ZrO_2}-W, \tag{4}$$

which follows from Eq. (3) by using the definition of the surface-interface tension for a given structure i from its total energy E_i:

$$E_i=\sigma_i+E_i^{\text{Bulk reference}}. \tag{5}$$

In this equation $E_i^{\text{Bulk reference}}$ is total energy of the structure i embedded in its appropriate reference bulk environment. Of course, this definition is only unique for stoichiometric and crystalline structures. The sign and magnitude of $\sigma_{ZrO_2||Al_2O_3}$ tells whether the interface bonds are stronger than the internal bonds in each ceramic, so that $0<\sigma_{ZrO_2||Al_2O_3}<\sigma_{Al_2O_3}+\sigma_{ZrO_2}$ corresponds to weakly coupled interfaces, and $\sigma_{ZrO_2||Al_2O_3}<0$ strongly coupled interfaces. A very negative $\sigma_{ZrO_2||Al_2O_3}$ may reflect a propensity to form an intermediate phase (chemically mixed) at the interface.

TABLE VI. Effect of straining the $t\text{-}ZrO_2$ films parallel to the surface from the square surface unit cell ($a_0=5.07$ Å), corresponding to cubic bulk, to accommodate the $\alpha\text{-}Al_2O_3(1\bar{1}02)$ substrate with a rectangular surface unit cell 4.76 Å×5.13 Å.

Layers $t\text{-}ZrO_2$	Strain energy (mJ/m^2)	Absolute slab dilation along [001] direction (Å)
1	11	0.03
2	124	0.12
3	323	0.08
4	488	0.11

Using $\sigma_{t-ZrO_2}=800$ mJ/m^2 and $\sigma_{Al_2O_3}=1000$ mJ/m^2 (approximate asymptotic values in Table II) gives $\sigma_{ZrO_2||Al_2O_3}\sim+600$ mJ/m^2. It would be slightly more correct to use σ_{m-ZrO_2} in Eq. (4), since even very thin $ZrO_2(001)$ films transform to a monoclinic structure, as is discussed in Sec. IV C. This quantity is not readily available from our calculations, due to the strained state of these films when constrained to the substrate lattice vectors as in our calculation, but a previous study of ZrO_2 surfaces[14] within the LDA for exchange-correlation effects suggests that the surface energy for $m\text{-}ZrO_2(001)$ is $\sim$200 mJ/m^2 higher than $t\text{-}ZrO_2(001)$. Whatever specific value is used for σ_{ZrO_2} the sign and magnitude of $\sigma_{ZrO_2||Al_2O_3}$ does not change. This is also in accordance with the two-component phase diagram[66] of ZrO_2/Al_2O_3, which shows that this system only displays entropy-driven mixing.

F. Interface strain

In this section we address the issue of strain in the deposited ZrO_2 film and the influence of strain on cohesion and structure. In Table VI we show the energy required to strain thin $t\text{-}ZrO_2$ films from the natural square lattice with the bulk lattice constant $a_0=5.07$ Å to the $\alpha\text{-}Al_2O_3(1\bar{1}02)$ coherent substrate cell with dimensions 4.76 Å×5.13 Å, see Sec. IV A. Ions are allowed to relax in both cases with the lattice constants fixed. The dilations perpendicular to the surface, measured from outermost anion to outermost anion on each side of the slab, are given in Table VI. Some even-odd oscillation with number of layers is present, which can be related to the fact that even- and odd-layered $t\text{-}ZrO_2(001)$ slabs have different symmetry, $P\bar{4}m2$ and $Pmmn$ for even- and odd-layered slabs, respectively (subsequent layers are not translational copies of each other, but related by a 90° screw or inversion operation). The strain energy for $m\text{-}ZrO_2(001)$ slabs forced into registry with the substrate is expected to be significantly larger, due to the large volume expansion accompanying the ($t\rightarrow m$) transition. Despite the compressive strain providing a driving force against the ($t\rightarrow m$) transition, the (incomplete) m phase is energetically preferred over the t phase, as discussed in Sec. IV C.

The magnitude of the strain energy in ZrO_2 films forced into registry with the $\alpha\text{-}Al_2O_3(1\bar{1}02)$ substrate, compared to

TABLE VII. Charge transfer (electrons/atom) projected onto atoms in the ZrO_2 and Al_2O_3 layers at the interface.

			Layers of ZrO_2 on $Al_2O_3(1\bar{1}02)$			
			1	2a[a]	2b[b]	3
	O		−0.01	−0.02	−0.03	0.00
		O	0.00	0.00	−0.02	−0.01
Interface ZrO_2 layer	Zr		0.03	0.00	−0.04	−0.02
		Zr	−0.07	−0.08	−0.17	−0.05
	O		0.05	0.04	0.06	0.06
		O	0.05	0.06	0.05	0.06
Interface plane						
	O		0.00	0.00	−0.01	−0.02
		O	0.00	0.00	−0.01	0.02
	Al		−0.06	−0.07	−0.07	−0.03
		Al	−0.05	−0.04	−0.02	−0.02
Interface Al_2O_3 layer	O		0.01	0.01	0.02	0.02
		O	0.00	0.00	0.01	0.01
	Al		0.01	0.00	0.03	0.02
		Al	0.00	0.00	0.02	0.03
	O		−0.01	−0.01	−0.01	−0.01
		O	−0.01	−0.01	0.00	0.00

[a] Two layers of ZrO_2, with structure corresponding to Fig. 7(a). See Sec. IV D for more details.

[b] Two layers of ZrO_2, with structure corresponding to Fig. 7(b). See Sec. IV D for more details.

the interface adhesion energy, suggests that only partial registry at the $ZrO_2(001)/\alpha\text{-}Al_2O_3(1\bar{1}02)$ interface is likely to be present at the real interface. This further suggests that dislocations may play a role in interface de-adhesion.

G. Charge distribution

In Table VII we display for each ion the approximate charge transfer upon interface formation, as function of the number of deposited ZrO_2 layers. In other words, from the charge on each ion in the interface region, we subtract the charge on the corresponding surface ion in the respective isolated oxide surface. These charges are obtained by spatial integration inside spheres around each ion, as discussed in Sec. II A. These spheres are not strictly space dividing, therefore charge conservation is not ensured, however some error cancellation is obtained when taking differences. Therefore we take these charge differences as a qualitative indicator of the charge transfer on forming the interface.

Generally, this interface formation is accompanied by almost no charge transfer. This is not surprising, because each oxide in our calculation is stoichiometric so that each ion remains mostly in its conventional charge state, due to oxygens large electron affinity. However, a minor trend is apparent: the cations closest to the interface on each side loses a small amount of charge, which is partly donated to the first oxygen atoms on the ZrO_2 side of the interface. The magnitude of charge redistribution within ions seems rather sensitive to the number of deposited ZrO_2 layers but is confined to the ions with direct interface contact.

H. Density-of-states at the interface

Figure 8 displays the total valence DOS for the interface structure with three layers $\alpha\text{-}Al_2O_3(1\bar{1}02)+$ three layers $ZrO_2(001)$. Juxtaposed are the DOS for the corresponding isolated $\alpha\text{-}Al_2O_3(1\bar{1}02)$ and $ZrO_2(001)$ surface slabs for comparison. The spectra for the interface structure and the respective surface slabs are shifted, so that the DOS, projected onto ions on the vacuum sides of the interface slab, is coincident with the DOS projected onto ions on the vacuum sides of the corresponding surface slabs—in other words, the spectra are aligned according to ions far from the physical interface, so that shifts in the DOS can be read off Fig. 8.

Figure 8 shows that $\alpha\text{-}Al_2O_3$ fixes the valence-band maximum whereas ZrO_2 defines the conduction-band mini-

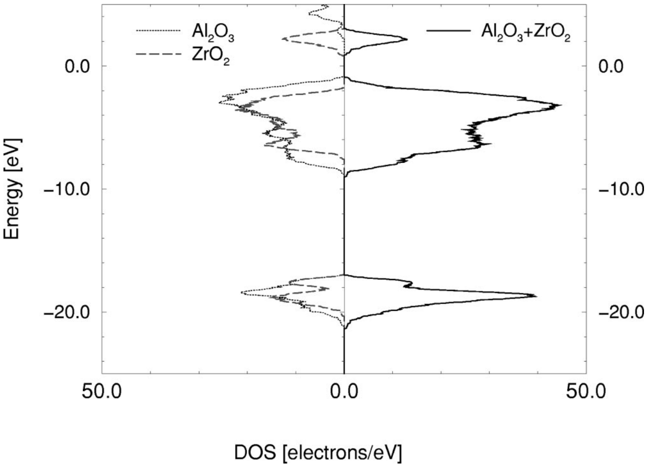

FIG. 8. Energy-resolved total density-of-states before and after the interface is formed. (Right) Total electronic valence density-of-states for an interface structure with three layers $\alpha\text{-}Al_2O_3(1\bar{1}02)$ + three layers $ZrO_2(001)$. (Left) Total electronic valence density-of-states for isolated surface slabs with three layers $\alpha\text{-}Al_2O_3(1\bar{1}02)$ and three layers $m\text{-}ZrO_2(001)$, respectively.

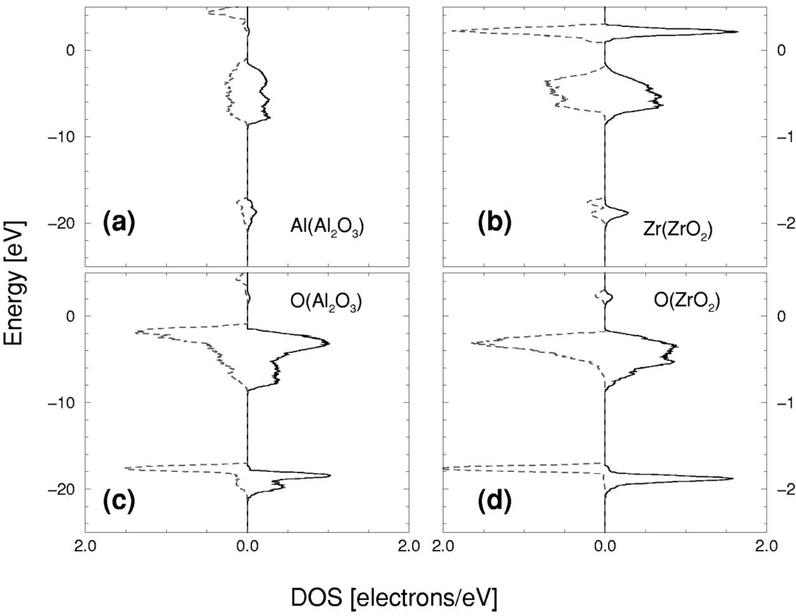

FIG. 9. In each graph (a)–(d), the right-hand side of each graph shows the density-of-states projected onto an interface ion, whereas the left-hand side of each graph shows the density-of-states projected onto the corresponding surface ion for the isolated α-Al$_2$O$_3$(1$\overline{1}$02) and ZrO$_2$(001) slabs. Thus, comparing left-hand and right-hand sides of each graph (a)–(d) gives an impression of the change in the energy-resolved density-of-states when forming the interface from isolated oxide surfaces. The surface ion density of states for ZrO$_2$(001) is taken from the most stable pseudomonoclinic ZrO$_2$(001) slab shown in Fig. 6(c).

mum in the interface structure. Therefore the interface structure has a smaller band-gap than either bulk material α-Al$_2$O$_3$ or ZrO$_2$. In a macroscopic structure, this band-gap narrowing will be confined to the physical interface region. It appears in Fig. 8 (right) that the Al$_2$O$_3$-derived conduction band has disappeared for the interface—this is due to the fact that only 6 empty bands are included in all our calculations, and for the interface structure these 6 empty bands will only represent the ZrO$_2$-derived conduction band on the ZrO$_2$ side. More unoccupied bands must be included for the Al$_2$O$_3$-derived conduction band to appear. This, however, has no effect on the occupied valence bands on either side of the interface.

Figure 9 displays the DOS projected onto representative interface ions on each side of the interface, compared to the DOS for the corresponding isolated surface ions. The interface DOS is derived from the three layers α-Al$_2$O$_3$(1$\overline{1}$02) + three layers ZrO$_2$(001) structure, while the surface DOS is from the corresponding isolated surface slabs. We apply same spectrum alignment procedure as in Fig. 8. Both isolated surface slabs are oxygen terminated, therefore the surface anions of both oxides experience significant stabilizing Madelung potential shifts, when the interface is formed. These Madelung shifts make a significant contribution to the cohesion, due to the relatively epitaxial character of the interface, see Fig. 4(a)–4(c) (in the same way as the Madelung potential is the main stabilizing component in ionic bonding). The Madelung shift is slightly larger for anions on the ZrO$_2$ side, monitoring the O($2s$)-derived states. This follows from simple steric considerations, because the anions on the Al$_2$O$_3$ side go from threefold to fourfold coordination on forming the interface, whereas the anions on the ZrO$_2$ side goes from twofold to threefold coordination by the interface formation, which is a larger relative change. In other words, trends in Madelung potential shifts are related to the relative compactness of α-Al$_2$O$_3$(1$\overline{1}$02) versus ZrO$_2$(001). This is also supported by the fact that valence-band width on the ZrO$_2$ interface anion is broadened more than the valence-band width on the Al$_2$O$_3$ anion, when the interface is formed. A weakly covalent conduction-band-valence-band interaction is visible, mediated through Zr to interface oxygen ions on the Al$_2$O$_3$ side—this is because the Al$_2$O$_3$ valence band lies higher than the ZrO$_2$ valence band and the ZrO$_2$ conduction band lies lower than the Al$_2$O$_3$ conduction band.

Figure 10 shows the DOS projected onto anions and cations at the interface and farther from the interface. Thus, Fig. 10 represents a primitive DOS profile across the interface region. The reference ‘‘bulk’’ ions are situated in approximately in the middle of each oxide in the interface structure. More specifically, they have the following distances from the interface (distance from the nearest surface given in parentheses): Al: 4.6 Å (5.2 Å), O (Al$_2$O$_3$ side): 4.2 Å (5.6 Å); Zr: 4.2 Å (4.0 Å), O (ZrO$_2$ side): 3.3 Å (4.8 Å). The DOS is extracted from the largest calculation, three layers α-Al$_2$O$_3$(1$\overline{1}$02)+ three layers ZrO$_2$(001).

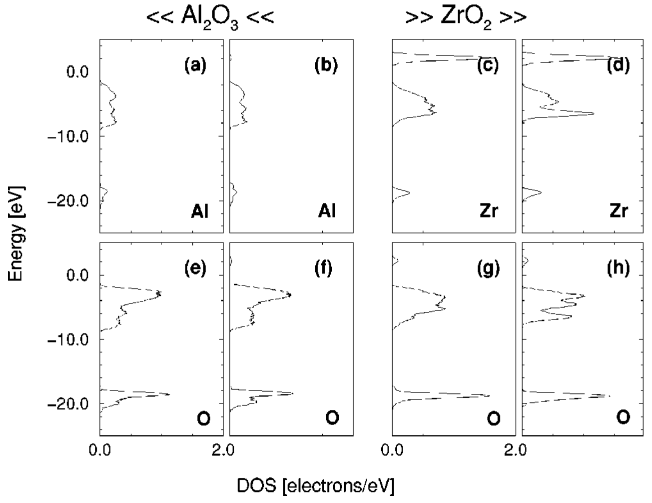

FIG. 10. Density-of-states (DOS) profile across the interface, projected onto both anions and cations close and farther from the physical interface. (a),(b),(e), and (f) are ions on the Al$_2$O$_3$ side of the interface, whereas (c),(d),(g), and (h) are ions on the ZrO$_2$ side of the interface. (a), (e) and (d), (h) corresponds to ions far from the interface. See the text for details.

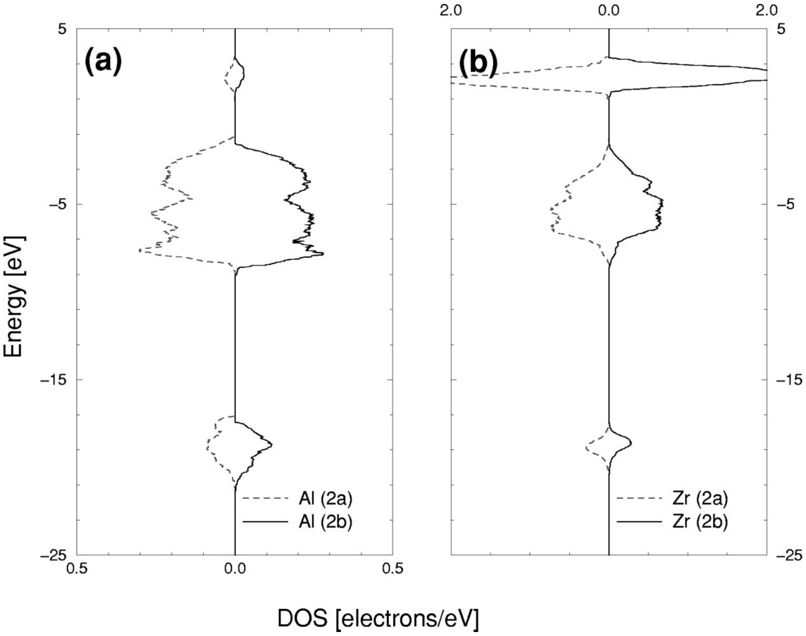

FIG. 11. Electronic density-of-states for interface cations in the two structures displayed in Fig. 7, each with three layers α-$Al_2O_3(1\bar{1}02)$ + two layers $ZrO_2(001)$. Each graph above compares corresponding ions from Figs. 7(a) and 7(b). (a) The density-of-states projected onto interface Al ions. (b) The density-of-states projected onto interface Zr ions. In both graphs, the legend (2a) refers to the structure in Fig. 7(a) and legend (2b) refers to the structure in Fig. 7(b). The interface in Fig. 7(b) is 0.09 eV/unit cell more stable than that in Fig. 7(a).

On the ZrO_2 side, the characteristic d features of the valence band are smoothened for the ions with direct interface contact. On the Al_2O_3 side, the DOS features for the interface ions are more similar to bulk Al_2O_3. The ZrO_2 conduction band around $+2$ eV has a visible tail on the Al_2O_3 side, which decays away as one moves further into the Al_2O_3 side. The average penetration depth for this tail is 2.0 Å, as determined from the integrated weight in the ion projected DOS spectrum. No band bending effects are visible. These would mainly appear as uniform shifts in the ion-projected DOS spectra.

Figure 11 depicts the DOS projected onto interface Al-Zr ions for the two interface structures displayed in Fig. 7 with two layers $ZrO_2(001)$ deposited. The structure in Fig. 7(b) has some Al-Zr coordination at the interface, as is apparent in Table IV and Fig. 7(b), whereas Al-Zr coordination is less prominent in the structure in Fig. 7(a). Figure 11 suggests some covalent Al-Zr interaction between the Al_2O_3 valence-band projection on Al and the ZrO_2 conduction band projection on Zr for the interface [Fig. 7(b)]. This interaction seems to increase the local band gap. Conversely, an Al_2O_3 conduction-band ZrO_2 valence-band interaction is not apparent for the coordinating Al-Zr pair in Fig. 7(b).

V. DISCUSSION

Our calculations show that m-$ZrO_2(001)$ is energetically favored over t-$ZrO_2(001)$ on the α-$Al_2O_3(1\bar{1}02)$ substrate. This is consistent with experiments.[16,19] On the α-$Al_2O_3(10\bar{1}2)$ substrate, Moulzolf *et al.*[21] also observed m-$ZrO_2(001)$ growth. However, for slow deposition rates on α-$Al_2O_3(10\bar{1}2)$, they observed c-$ZrO_2(001)$ to grow in films up to 400 Å thick. This is an intriguing observation, because our electronic structure calculations show that bulk c-ZrO_2 can undergo a barrierless transformation to quasi-t-ZrO_2 at low temperatures *even* if the unit cell is frozen to the dimensions of bulk c-ZrO_2; this leaves open the possibility that c-$ZrO_2(001)/\alpha$-$Al_2O_3(10\bar{1}2)$ is entropy stabilized. An energetic order-of-magnitude argument suggests that it is unlikely the c-$ZrO_2(001)$ α-$Al_2O_3(10\bar{1}2)$ should be absolutely stable over m-$ZrO_2(001)/\alpha$-$Al_2O_3(10\bar{1}2)$. Taking the $(c\rightarrow m)$-ZrO_2 potential transformation energy release to be ~ 0.06 eV/ion translates to 90 mJ/m^2 per Å thickness in a ZrO_2 film. Comparing this to the order of magnitude of *differences* in surface and interface energies leaves it unlikely that c-ZrO_2-films up to 400 Å thick on α-Al_2O_3 should be globally stable at low temperatures. This corresponds to $\sim 36\,000$ mJ/m^2 releasable bulk energy, of which a small amount can be used to compensate for an unfavorable interface coordination. Thus, we believe the deposited c-$ZrO_2(001)$ films ultimately transform into m-$ZrO_2(001)$ upon thermal cycling. Likewise, the nanolaminate t-ZrO_2 amorphous Al_2O_3 structures studied by Scanlan *et al.*[22] are likely to be kinetically stabilized. The polycrystalline nature of the nanolaminates may serve to stabilize small crystallites of t-ZrO_2, as we have suggested previously.[14]

VI. CONCLUSIONS

We have studied the $ZrO_2(001)||\alpha$-$Al_2O_3(1\bar{1}02)$ interface using the all-electron PAW formalism and a GGA functional for exchange-correlation effects. We characterize this interface as weakly coupled, but relatively epitaxial, due to the small lattice-constant mismatch between $ZrO_2(001)||\alpha$-$Al_2O_3(1\bar{1}02)$. Three out of four anion-cation bonds, which are broken when forming each of the α-$Al_2O_3(1\bar{1}02)$ and $ZrO_2(001)$ surfaces, are reestablished when the $ZrO_2(001)||\alpha$-$Al_2O_3(1\bar{1}02)$ interface is formed. Rather interestingly, we find that a stabilizing (screened) cation-cation interaction across the interface is possible, where the Al-Zr distance across the interface is 0.15 Å shorter than the average cation-cation distances for these oxides. This could be due to interactions of the remaining Zr d electrons with empty sp states on the Al cations. It is questionable whether this slightly counterintuitive feature will be reproduced by semiempirical model potentials currently available for modeling ionic materials. The covalent effects at this interface are found to be relatively weak, though. The calculated adiabatic work of adhesion is ~ 1200 mJ/m^2, and this value is roughly independent of the number of deposited $ZrO_2(001)$ layers. In other words, the interface chemistry is local for this interface, whereas the elastic misfit energy depends on the thickness of the deposited $ZrO_2(001)$ film. The weakness of the alumina-zirconia interface is consistent with the observed deadhesion of the Ni-Al-Cr-Y bond coat/ZrO_2 interface upon oxidation of the bond coat to produce a thin layer of Al_2O_3.

Thin tetragonal $ZrO_2(001)$ films are predicted to undergo an incomplete monoclinic transition, even when subjected to compressive strain. $ZrO_2(001)$ with three layers are seen to have the characteristic sevenfold cation coordination and alternating threefold and fourfold anion coordination for the middle layer; this is not possible for one- and two-layered $ZrO_2(001)$ films, but characteristic monoclinic precursor structures are found in these cases. We find it unlikely that the incomplete tetragonal → monoclinic transition is strain induced, due to the fact that the strain is compressive and that the tetragonal → monoclinic transition accompanied by a 4% volume increase. We find that ZrO_2 adhesion onto the α-$Al_2O_3(1\bar{1}02)$ surface is not sufficient to suppress the tetragonal → monoclinic transition, even as it induces significant compressive strain in the ZrO_2 overlayer, due to the larger specific volume of the monoclinic ZrO_2 phase.

We investigate the effect of finite Al_2O_3-substrate thickness and find that in most respects, for electronic structure as well as for structural aspects, a film thickness of ~ 10 Å is sufficient to emulate the infinite Al_2O_3 substrate, as long as the surface lattice vectors of Al_2O_3 are kept fixed to prevent artificial substrate creep parallel to the surface.

We find that GGA, compared to LDA, for exchange-correlation effects within density-functional theory significantly lower the surface energies for both Al_2O_3 and ZrO_2, which bring their values closer to those implied by experiments. Conversely, we find that GGA functionals overestimate structural energy differences between bulk phases of ZrO_2, although the phase stability ordering is correct.

The study of complex structures like the $ZrO_2||\alpha$-$Al_2O_3(1\bar{1}02)$ interface illustrates the importance of annealing via molecular-dynamics simulations. Many competing, locally stable, interface structures exist, and it is important to heat up and requench the relaxed interface to make sure that the system has not been caught in an energetically unfavorable local minimum.

The low adhesion energy is probably due to the fact that these surfaces of ZrO_2 and Al_2O_3 relax to obtain approximate coordinative saturation and therefore the lack of dangling bonds on these surfaces minimizes the interaction they have between them. This suggests that the role of the Al_2O_3 in the nanolaminate coatings is simply to act as a physical barrier to growth of the ZrO_2 layer and that there is no true chemical bonding between these layers. Further, this weak interaction has important implications for thermal barrier coatings. When the bond coat oxidizes, it is known that Al_2O_3 forms and that the lifetime of the TBC is tied to the oxidation kinetics of the bond coat.[2,6,67–70] A microscopic explanation, based on our findings above, is now available; there is a weak interaction between ZrO_2 and Al_2O_3, and thus ZrO_2 deadheres when this interface is formed. In other work,[12] we have determined that Al_2O_3-Ni interfaces are also quite weakly adhered, suggesting spallation occurs at any interface in the TBC where Al_2O_3 is present.

With our *ab initio* calculations, insight into the local bonding and structure for the ZrO_2-Al_2O_3 interface has been obtained. Still, many physical properties of interfaces are governed by long-ranged effects, such as domain structures, or by events occuring on long-time scales, such as ionic diffusion. This requires very large atomistic ensembles or very long-time trajectories to model, which are intractable with conventional *ab initio* molecular-dynamics simulations. This put emphasis on combining *ab initio* techniques with multiscale modeling and Monte Carlo schemes, and/or developing transferable semiempirical interatomic potentials beyond shell-model potentials.

ACKNOWLEDGMENTS

We are very grateful to Peter E. Blöchl for use of his CP-PAW code and many useful and inspiring discussions, as well as advice on the PAW-Car-Parrinello method. Further we wish to thank Niranjan Govind, Stuart C. Watson, and Emily A. A. Jarvis for useful comments. We acknowledge also computing time granted on the parallel IBM SP2 platforms at the Maui High-Performance Computing Center (MHPCC) and the Office of Academic Computing, UCLA. This work was supported by the Air Force Office of Scientific Research (Grant No. F49620-96-1-0064).

---

*Email address: asbjorn@chem.ucla.edu
†Email address: eac@chem.ucla.edu

[1] A. Christensen, E.A.A. Jarvis, and E.A. Carter, in *Chemical Dynamics in Extreme Environments*, edited by R.A. Dressler and C. Ng, Advanced Series in Physical Chemistry (World Scientific, Singapore, 2000).

[2] D.J. Wortman, B.A. Nagaraj, and E.C. Duderstadt, Mater. Sci. Eng., A **121**, 433 (1989).

[3] S.M. Meier, D.K. Gupta, and K.D. Sheffler, J. Miner. Metal Mater Soc. **43**, 50 (1991).

[4] E. Ryshkewitch and D.W. Richerson, *Oxide Ceramics* (Academic Press, Orlando, 1985).

[5] S. Musikant, *What Every Engineer Should Know About Ceramics* (Marcel Dekker, New York, 1991).

[6] F.H. Stott, D.J. de Wet, and R. Taylor, MRS Bull. **19**(10), 46 (1994).

[7] Y.H. Sohn, R.R. Biederman, and R.D. Sisson, Jr., J. Mater. Eng. Perform. **3**, 55 (1994).

[8] R. Taylor, J.R. Brandon, and P. Morrell, Surf. Coat. Technol. **50**, 141 (1992).

[9] A.E. Hughes, in *Science of Ceramic Interfaces II*, edited by J. Nowotny (Elsevier, Amsterdam, 1994).

[10] W. Lih, E. Chang, B.C. Wu, and C.H. Chao, Oxid. Met. **36**, 221 (1991)0.

[11] R.A. Miller, J. Am. Ceram. Soc. **67**, 517 (1984).

[12] E.A.A. Jarvis, A. Christensen, and E.A. Carter (unpublished).

[13] A. Christensen and E.A. Carter, J. Chem. Phys. (to be published).

[14] A. Christensen and E.A. Carter, Phys. Rev. B **58**, 8050 (1998).

[15] G. Stapper, M. Bernasconi, N. Nicoloso, and M. Parrinello, Phys. Rev. B **59**, 797 (1999).

[16] X.D. Wu, R.E. Muenchausen, N.S. Nogar, A. Pique, R. Edwards, B. Wilkens, T.S. Ravi, D.M. Hwang, and C.Y. Chen, Appl. Phys. Lett. **58**, 304 (1991).

[17] G. Garcia, J. Casado, J. Llibre, A. Figueras, S. Schamm, D. Dorignac, and Ch. Grigis, *Proceedings of the Thirteenth International Conference on Chemical Vapor Deposition (CVD XIII)*, edited by T.M. Besmann, M.D. Allendorf, McD. Robinson, and R.K. Ulrich, Electrochemical Society (Pennington, NJ, 1996) p. 699–705.

[18] L.F. Chen, P.F. Chen, L. Li, S.L. Li, X.N. Jing, S.J. Pan, and Y.H. Guo, Appl. Phys. Lett. **61**, 2412 (1992).

[19] F. Konushi, T. Doi, H. Matsunaga, Y. Kakihara, M. Koba, K. Awane, and I. Nakamura, Mater. Res. Soc. Symp. Proc. **56**, 259 (1986).

[20] M.G. Cain and F.F. Lange, J. Mater. Res. **9**, 674 (1994).

[21] S.C. Moulzolf, Y. Yu, D.J. Frankel, and R.J. Lad, J. Vac. Sci. Technol. A **15**, 1211 (1997).

[22] C.M. Scanlan, M. Gajdardziska-Josifovska, and C.R. Aita, Appl. Phys. Lett. **64**, 3548 (1994).

[23] P.E. Blöchl, Phys. Rev. B **50**, 17 953 (1994).

[24] P. Hohenberg and W. Kohn, Phys. Rev. **136**, B864 (1964); W. Kohn and L. Sham, Phys. Rev. **140**, A1133 (1965).

[25] N.A.W. Holzwarth, G.E. Matthews, R.B. Dunning, A.R. Tackett, and Y. Zeng, Phys. Rev. B **55**, 2005 (1997).

[26] G. Kresse and D. Joubert, Phys. Rev. B **59**, 1758 (1999).

[27] H.J.F. Jansen, Phys. Rev. B **43**, 7267 (1991).

[28] J.P. Perdew and A. Zunger, Phys. Rev. B **23**, 5048 (1981).

[29] A.D. Becke, J. Chem. Phys. **96**, 2155 (1992).

[30] J.P. Perdew, Phys. Rev. B **33**, 8822 (1986).

[31] R. Car and M. Parrinello, Phys. Rev. Lett. **55**, 2471 (1985).

[32] L. Verlet, Phys. Rev. **159**, 98 (1967).

[33] O.H. Nielsen and R.M. Martin, Phys. Rev. B **32**, 3780 (1985); **32**, 3792 (1985).

[34] S. Froyen and M.L. Cohen, J. Phys. C **19**, 2623 (1986); D. Vanderbilt, Phys. Rev. Lett. **59**, 1456 (1987).

[35] S. Nosé, J. Chem. Phys. **81**, 511 (1984).

[36] R.W.G. Wyckoff, *Crystal Structures*, 2nd ed. (Interscience Publishers, New York, 1963), Vols. 1 and 2.

[37] H.J.F. Jansen and J.A. Gardner, Physica B & C **150**, 10 (1988).

[38] R.H. French, S.J. Glass, F.S. Ohuchi, Y.-N. Xu, and W.Y. Ching, Phys. Rev. B **49**, 5133 (1994).

[39] B. Kralik, E.K. Chang, and S.G. Louie, Phys. Rev. B **57**, 7027 (1998).

[40] G. Jomard, T. Petit, A. Pasturel, L. Magand, G. Kresse, and J. Hafner, Phys. Rev. B **59**, 4044 (1999).

[41] R. Orlando, C. Pisani, C. Roetti, and E. Stefanovich, Phys. Rev. B **45**, 592 (1992).

[42] E.V. Stefanovich, A.L. Shluger, and C.R.A. Catlow, Phys. Rev. B **49**, 11 560 (1994).

[43] M.W. Finnis, A.T. Paxton, M. Methfessel, and M. van Schilfgaarde, Phys. Rev. Lett. **81**, 5149 (1998).

[44] M. Wilson, U. Schonberger, and M.W. Finnis, Phys. Rev. B **54**, 9147 (1996).

[45] C.J. Howard, R.J. Hill, and B.E. Reichert, Acta Crystallogr., Sect. B: Struct. Sci. **44**, 116 (1988).

[46] G. Teufer, Acta Crystallogr. **15**, 1187 (1962).

[47] *International Tables for Crystallography*, edited by T. Hahn (Kluwer Academic, Boston, 1996), Vol. A.

[48] M.W. Finnis, J. Phys.: Condens. Matter **8**, 5811 (1996).

[49] C. E. Moore, *Atomic Energy Levels* (Washington, U.S. GPO, DC, 1958), Vols. 1–3.

[50] R.O. Jones and O. Gunnarsson, Rev. Mod. Phys. **61**, 689 (1989).

[51] M.M. Abou Sekkina, Indian J. Phys., A **52A**, 244 (1978); R.S. Sokolova, Sov. J. Appl. Phys. **41**, 454 (1974).

[52] R.H. French, J. Am. Ceram. Soc. **73**, 477 (1990).

[53] R. Stevens, *Zirconia and Zirconia Ceramics* (Magnesium Elektron Ltd., London, 1986).

[54] G. Kresse and J. Hafner, Phys. Rev. B **47**, 558 (1993); **49**, 14 251 (1994); G. Kresse and J. Furthmüller, Comput. Mater. Sci. **6**, 15 (1996); G. Kresse and J. Furthmüller, Phys. Rev. B **55**, 11 169 (1996).

[55] J.P. Perdew, in *Electronic Structure of Solids*, edited by P. Ziesche and H. Eschrig (Akademie-Verlag, Berlin, 1991), p.11; J.P. Perdew, J.A. Chevary, S.H. Vosko, K.A. Jackson, M.R. Pederson, D.J. Singh, and C. Fiolhais, Phys. Rev. B **46**, 6671 (1992).

[56] J. Guo, D.E. Ellis, and D.J. Lam, Phys. Rev. B **45**, 13 647 (1992).

[57] V.E. Henrich and P.A. Cox, *The Surface Science of Metal Oxides* (Cambridge University Press, Cambridge, 1994).

[58] R. Orlando, C. Pisani, E. Ruiz, and P. Sautet, Surf. Sci. **275**, 482 (1992).

[59] J. Goniakowski, J.M. Holender, L.N. lKantorovich, M.J. Gillan, and J. White, Phys. Rev. B **53**, 957 (1996).

[60] S.P. Bates, G. Kresse, and M.J. Gillan, Surf. Sci. **385**, 386 (1997).

[61] I. Manassidis and M.J. Gillan, J. Am. Ceram. Soc. **77**, 335 (1994).

[62] M. Causa, R. Dovesi, C. Pisani, and C. Roetti, Surf. Sci. **215**, 259 (1989).

[63] C.T. Campbell, Surf. Sci. Rep. **27**, 1 (1997).

[64] A. Tsoga and P. Nikolopoulos, J. Mater. Sci. **31**, 5409 (1996).

[65] G.K. Bansil and A.H. Heuer, Acta Metall. **20**, 1281 (1972); **22**, 409 (1974).

[66] G.R. Fisher, L.I. Manfredo, R.N. McNally, and R.C. Doman, J. Mater. Sci. **16**, 3447 (1970).

[67] W. Lih, E. Chang, C.H. Chao, and M.L. Tsai, Oxid. Met. **38**, 99 (1992).

[68] M.W. Brumm and H.J. Grabke, Corros. Sci. **33**, 1677 (1992).

[69] T.K. Gupta, J.H. Bectold, R.C. Kuznicki, L.H. Cadoff, and B.R. Rossing, J. Mater. Sci. **12**, 2421 (1977).

[70] S.M. Meier and D.K. Gupta, J. Eng. Gas Turbines Power **116**, 250 (1994).